 doi:10.20944/preprints202209.0036.v1

Article

Z2-γ: an Application of Zienkiewicz-Zhu Error Estimator to Brain Tumor Detection in MR Images.

Antonella Falini[1,*]

[1] Computer Science Department, University of Bari, Aldo Moro, Italy
* Correspondence: antonella.falini@uniba.it;

Abstract: Brain tumors are abnormal cells growth in the brain tissues that can be cancerous, or not. In any case, they could be a very aggressive disease that should be detected as early as possible. Usually, magnetic resonance imaging (MRI) is the main tool commonly adopted by neurologists and radiologists to identify and classify any possible anomalies present in the brain anatomy. In the present work, an automatic unsupervised method called Z2-γ, based on the use of adaptive finite-elements and suitable pre-processing and post-processing techniques, is introduced. In particular, the proposed methodology is able to automatically classify whether a given MR image represents a healthy or a diseased brain and in this latter case, is able to locate the tumor area.

Keywords: brain tumor detection; finite-elements; adaptivity; morphological transformation

1. Introduction

The term brain tumor refers to an abnormal growth of cells in the brain, it could be cancerous or not and could originates directly from the brain tissues or having a metastatic nature. Benign brain tumors have a uniform structure and do not contain active cells; on the contrary, malignant brain tumors have a non-uniform structure and contains active (cancerous) cells. All the types of brain tumors may produce symptoms that vary according to the involved parts of the brain. Moreover, brain tumors may vary in size and location, besides presenting a lot of abnormalities which make it difficult to characterize them and to identify them.

Magnetic Resonance Imaging (MRI) is a very common tool used in neurology for visualizing the brain anatomy along three different planes: axial, coronal and sagittal. When protons are placed in a magnetic field they align. This alignment (magnetization) is then perturbed by introducing an external radio frequency energy. The protons start oscillating and at this state they can absorb energy and hence, the nuclei can release it or re-radiate it. The nuclei then return to their original equilibrium state: the time that it takes to the relaxation of the component parallel to the magnetic field to go back to the equilibrium is called longitudinal relaxation time or T1; on the other hand, the transversal relaxation time is abbreviated with T2. The transmitted signals are measured, then, the Fourier transform is used to convert the frequency information to corresponding gray scale intensity values; this makes possible to construct an image. By varying the sequence of the radio frequency pulses applied and collected, different type of images can be created. In particular, calling by repetition time (RT) the time interval between successive pulse sequences applied to the same slice and calling by time to echo (RE) the time interval between the delivery of the pulse and the receiving of the echo signal, the so called T1-weighted and T2-weighted images can be created. In particular, T1-weighted are produced using short TE and TR, while T2-weighted are produced using longer TE and TR.

The objective of this paper is to describe a methodology which is able to identify any possible brain tumor given either a T1-weighted or a T2-weighted MRI. By screening the given image, the proposed approach is also able to locate the tumor area as well as to identify those scans that do not present any abnormal tissues, and hence, can be

Preprints (www.preprints.org) | NOT PEER-REVIEWED | Posted: 2 September 2022 doi:10.20944/preprints202209.0036.v1

categorized as healthy brains. The method here described relies on the use of a finite-elements approximation of the input image and on the use of the Zienkiewicz-Zhu (Z2) error estimator [1–3] to adaptively and locally refine the resolution of the image at specific sites.

While the use of finite-elements and adaptive strategies is not new in the image segmentation context, see e.g. [4–8], those methods are rather complex as they are framed in a variational formulation and their objective is different from the one proposed here: the given image is split in several parts or components that can be easily identified via the location of edges. Hence those methodologies aim at locally reconstructing the profiles of these regions, but they do not address the problem of the classification of such regions.

The method introduced here can can be interpreted as an unsupervised anomaly detection technique. Besides using the Z2 error estimator, it also exploits specific γ corrections according to which modality of MRI is analyzed, i.e., either T1-weighted or T2-weighted. As a final step, the use of morphological operators help to get rid of redundant noise and to locate the affected, i.e., anomalous, areas inside the brain tissues.

In general, regarding the brain tumor detection task, many methods are developed by using statistical and machine learning techniques, see e.g., [9,10]. In particular, more advanced architectures like convolutional neural networks (NN) [11], probabilistic NN [12,13], deep NN [14] and U-Nets [15] have been successfully applied to the task of image segmentation and brain tumor classification. On the other hand, many unsupervised methods exist as well; some are based on clustering techniques, [16–21]; others are based on automatic thresholding methods and morphological transformations, [22–26]. Some techniques apply a suitable projection in lower dimensional spaces in order to get rid of unwanted redundancies, and so classical matrix decompositions like the SVD or the non-negative matrix factorization are applied, see e.g., [27]. Histogram-based gravitational optimization algorithm [28], Gabor-wavelets [29] and other big data analytics techniques are also employed see [30] and references therein for a review. Many other approaches are based on anomaly detection: the main goal is to identify abnormalities, given only normal data in the training set, see e.g., [31–36]. Recent approaches have also exploited genetic and evolutionary algorithms, see [37] and references therein.

The present paper is organized as follows. In Section 2 the finite-elements mathematical framework is described. In Section 3 the adopted pre-processing and post-processing are discussed. In Section 4 the method is tested and compared with other available techniques. In Section 5 follows some conclusive remarks.

2. Mathematical Framework

Provided as input an MR image $\mathcal{I}$ having size $m \times n$ pixel, the following methodology produces a finite-element approximation on a locally refined regular triangulation. In particular, a denser number of triangles will be automatically located where the anomalous tissues are present, allowing for an easy detection of such regions. The first step consists in constructing a regular quadrangular grid associated to $\mathcal{I}$, i.e., every pixel is a node in such a grid. Then, every regular square is diagonally divided in two subtriangles. In this way we get a non overlapping regular triangulation $\mathcal{T}_h$ where h denotes the maximal diameter of the triangular elements. At this early stage, we have $h_T = diam(T) = h$ constant for every triangle $T \in \mathcal{T}_h$. More in general, $diam(T) := \max_{x,y \in T} \|x - y\|$ and hence, $h := \max_{T \in \mathcal{T}_h} h_T$. On the constructed triangulation, the space of linear finite-element can be defined,

$$V_h^1 := \left\{ v_h \in C^0(\bar{\Omega}) : v_{h|_T} \in \mathbb{P}_1, \forall T \in \mathcal{T}_h \right\}, \tag{1}$$

where $\Omega := (0, m) \times (0, n)$; $\mathbb{P}_1$ is the space of polynomials of degree less or equal to 1, and hence, V_h^1 denotes continuous piece-wise linear polynomial functions on every triangle T.

Preprints (www.preprints.org) | NOT PEER-REVIEWED | Posted: 2 September 2022 doi:10.20944/preprints202209.0036.v1

Every function $v_h \in V_h^1$ can be expressed as a linear combination of the basis functions $\{\varphi_k\}$ as,

$$v_h(\mathbf{x}) = \sum_{k=1}^{N_h} v_k \varphi_k(\mathbf{x}), \tag{2}$$

with v_k values of the function v_h at the grid nodes and N_h total number of grid nodes in $\mathcal{T}_h$. In our case, a continuous approximation image I is constructed by interpolating the original image $\mathcal{I}$ at the provided pixel values, i.e., via using expression (2),

$$I(\mathbf{x}) = \sum_{k=1}^{N_h} \mathcal{I}_k \varphi_k(\mathbf{x}), \tag{3}$$

where a linear global index k is used to identify every pixel (i, j) in $\mathcal{I}$, according to the mapping shown in Figure 1, and, again, N_h denotes the total number of nodes in $\mathcal{T}_h$.

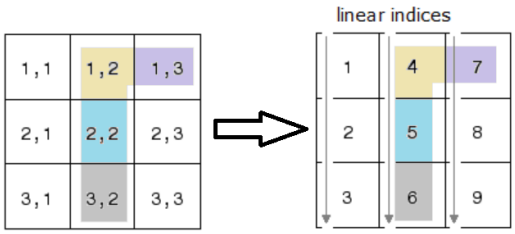

Figure 1. Mapping from classical two subscripts notation of matrix elements to global linear indexing.

As a second step, a downsampling of the constructed approximation I is performed. In particular, I is approximated itself via using a coarser triangulation $\widetilde{\mathcal{T}}_{\tilde{h}}$ having $\widetilde{N}_{\tilde{h}}$ vertices, where the set of these nodes is not necessarily a subset of the original triangulation nodes. This new approximation will be denoted as $\widetilde{I}_{\tilde{h}}$. The third step consists in computing the Zienkiewicz-Zhu error estimator $\eta_{\widetilde{T}}$ on every triangle $\widetilde{T} \in \widetilde{\mathcal{T}}_{\tilde{h}}$:

$$\eta_{\widetilde{T}} := \|G(\widetilde{I}_{\tilde{h}}) - \nabla \widetilde{I}_{\tilde{h}}\|_{L^2(\widetilde{T})}. \tag{4}$$

In our case, the function $G(\widetilde{I}_{\tilde{h}})$ is constructed by evaluating the function $\nabla \widetilde{I}_{\tilde{h}}$ on the barycenter of each triangle and then, by averaging on those triangles which share a common vertex. In particular, the reconstruction $G_{\tilde{k}}$ of the gradient at every node $\tilde{k}$ of the triangulation $\widetilde{\mathcal{T}}_{\tilde{h}}$ is done by,

$$G_{\tilde{k}} := \sum_{\widetilde{T} \ni \tilde{k}} \frac{|\widetilde{T}|}{|T_{\tilde{k}}|} \nabla \widetilde{I}_{\tilde{h}}|_{\widetilde{T}}, \tag{5}$$

where the symbol $|\cdot|$ in formula (5) denotes the area of the considered element and $T_{\tilde{k}}$ denotes the union of the triangles which share the vertex $\tilde{k}$. The elements $\widetilde{T}$ having a bigger $\eta_{\widetilde{T}}$ are the ones where the intensity value of the pixels varies the most. Then the estimators for every triangle are sorted from the smallest to the biggest one and the triangles that are marked, and hence, refined are the ones such that,

$$\eta_{\widetilde{T}} \geqslant c_{ref} \eta_{\widetilde{T}_t}, \tag{6}$$

with $t := pN_t$, N_t the total number of triangles and p percentage of triangles that will be considered; while $0 < c_{ref} < 1$. The marking strategy is fundamental to guarantee a specific order of convergence for the chosen approximant, see e.g., [38,39], however this is not the

Preprints (www.preprints.org) | NOT PEER-REVIEWED | Posted: 2 September 2022 doi:10.20944/preprints202209.0036.v1

main concern to be addressed for the current application. The parameters settings for the tests have been experimentally carried out.

Remark 1. *Although more accurate formulas exist for the gradient recovery estimation (see e.g, [40–43]), in this work, the choice of Eq. (5) is intentional: a more rough approximation is indeed preferable in this context rather than an extremely accurate one, as the main goal of the proposed methodology is to estimate the region extension of any possible anomalous tissue, rather than just delineating the profile or the edges of such regions.*

The refinement strategy is repeated for several iterations, until the maximum $\eta_{\widetilde{T}}$ does not reach the chosen threshold value, producing every time an isotropic triangulation. At the end, smaller triangles will be located in the regions of interest. Therefore, a final binary map b is produced by constructing $b \in V^0_{\widetilde{h}}$ as a piece-wise constant polynomial function, which is defined as,

$$b_{|\widetilde{T}} := \begin{cases} 1 & \text{if } |\widetilde{T}| \text{ is minimal,} \\ 0 & \text{otherwise.} \end{cases} \tag{7}$$

It should be noticed that having an isotropic triangulation is a fundamental step in order to produce feasible results with the described strategy. Indeed, having an anisotropic triangulation does not necessarily guarantee that the regions of interests are covered with triangles of small area. The shape of the triangles can be rather elongated and flattened, preventing from using the rule in (7) to produce a suitable binary map b.

2.1. A metastatic brain tumor example

To make the described procedure clearer to the reader, the following example shows the various employed steps. An image 283×295 pixels of a metastatic brain tumor is selected, Fig. 2 (a). The first interpolant I, obtained with linear finite-element and defined with 27828 degrees of freedom (dof), is shown in Fig. 2 (b), while the starting approximation $\widetilde{I}_{\widetilde{h}}$ for the conducted analysis, on a downsampled triangulation consisting of $N_t = 1200$ triangles and 217 dof, is shown in Fig. 2 (c). The triangulation is locally refined by using the error estimator in Eq.(4) and setting the parameters $p = 0.25$ and $c_{ref} = 0.60$ for the Eq. (6). The output of this process in shown in Fig. 2 (d) and (e), where the produced approximant $\widetilde{I}_{\widetilde{h}}$ is defined with 936 dof. In Fig. 2 (f), only for visualization purpose, the original MRI bright regions are superimposed to the final triangulation in order to show the coherence of the obtained results. Finally, in Fig. 2 (g) the final triangulation is shown again, but the triangles are colored according to their area value. In Fig. 2 (h) the produced binary map b is constructed from the final triangulation by selecting only the triangles with minimal area and setting the corresponding pixels to 1, while setting any other pixel value equal to 0. It is evident how there is still some noise affecting the quality of the produced results. Therefore, this final image will be post-processed as described in Section 3.2.

3. Experimental Results

The proposed method refines areas around those pixels where there is a relevant change in the gray intensity values. Therefore, it is prone to increase the resolution of the triangulation near extremely bright regions, or near extremely dark regions when the surrounding pixels have lower and higher intensity values, respectively. Given an MR-T1 or MR-T2 image, bright areas, as well as dark ones, are not necessarily neoplasic tissues. In order to avoid to refine unnecessary areas and to give a false prediction for an healthy brain, it is convenient to pre-process the images as follows.

3.1. Pre-processing

Every gray MR acquired image is firstly scaled in the interval $[0, 1]$. Then, in order to reduce the difference in intensity values that could occur around healthy regions, that

Preprints (www.preprints.org) | NOT PEER-REVIEWED | Posted: 2 September 2022 doi:10.20944/preprints202209.0036.v1

(a) Given MRI scan $\mathcal{I}$.

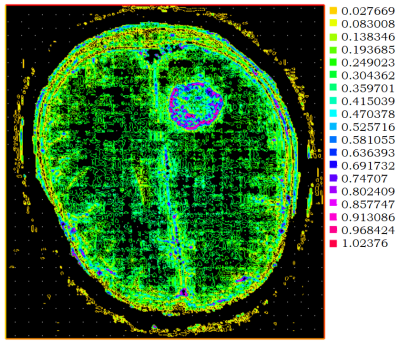

(b) Image interpolated I.

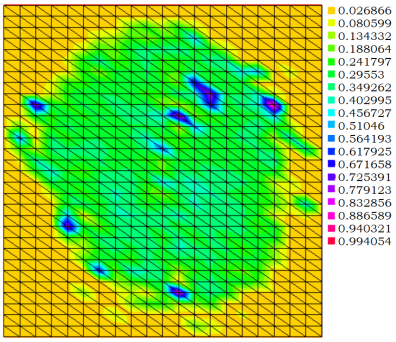

(c) Initial $\widetilde{I}_{\widetilde{h}}$ on the initial grid.

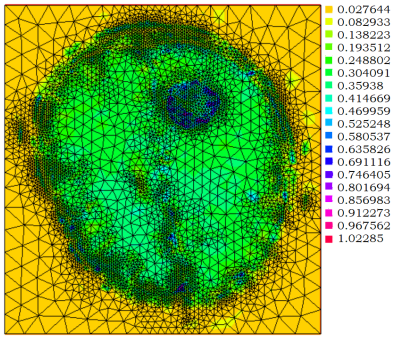

(d) Final $\widetilde{I}_{\widetilde{h}}$ on the final $\widetilde{\mathcal{T}}_{\widetilde{h}}$.

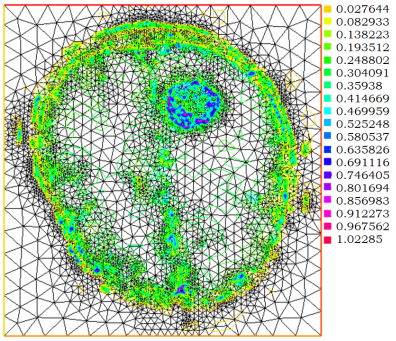

(e) Isolines of the final $\widetilde{I}_{\widetilde{h}}$ and final $\widetilde{\mathcal{T}}_{\widetilde{h}}$.

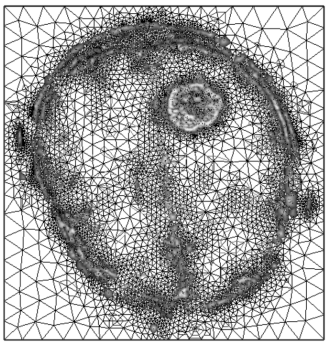

(f) Initial MRI superimposed to the final $\widetilde{\mathcal{T}}_{\widetilde{h}}$.

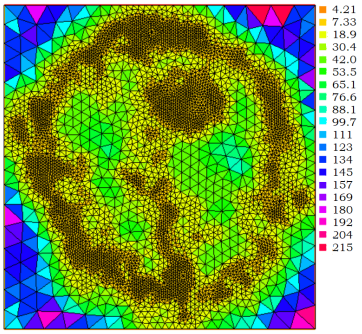

(g) Area of the triangles in the final $\widetilde{\mathcal{T}}_{\widetilde{h}}$.

(h) Binary map b obtained from Eq. (7).

Figure 2. Exemplification of the procedure described in Section 2.

otherwise would be detected as anomalous, a simple gamma correction is applied. More in detail, given $\mathcal{I}$ a gray image scaled in $[0, 1]$, the following transformation is applied:

$$\mathcal{G} := \mathcal{I}^{\gamma},$$

Preprints (www.preprints.org) | NOT PEER-REVIEWED | Posted: 2 September 2022 doi:10.20944/preprints202209.0036.v1

with $\gamma = 4$. The results can be visually appreciated in Figure 3. In particular, it is evident how for an healthy brain, Fig. 3(a), the gamma correction would make any pixel intensity value uniform besides the external cortex, see Fig. 3(b); while for an affected brain, Fig. 3(c), the neoplasic region would still be enhanced and hence detected, see Fig. 3(d).

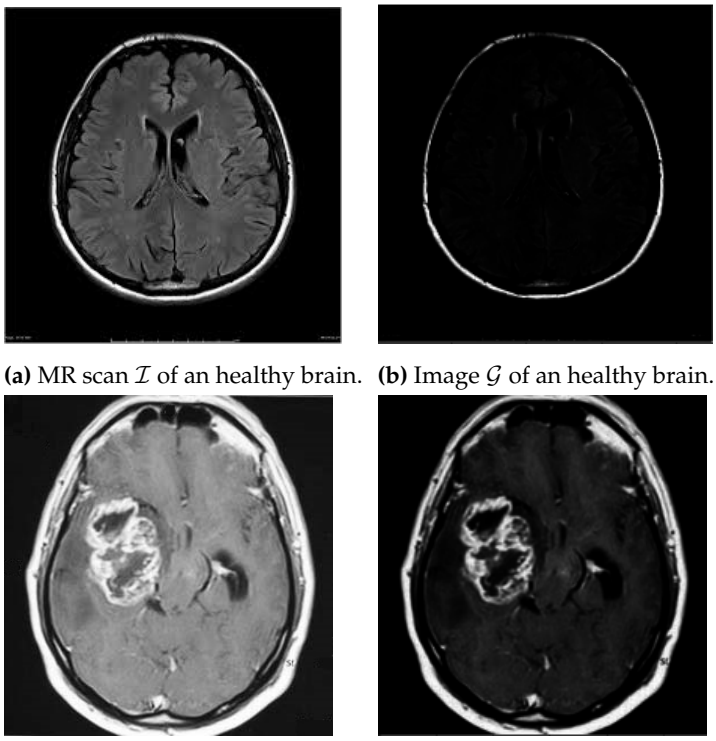

(a) MR scan $\mathcal{I}$ of an healthy brain. **(b)** Image $\mathcal{G}$ of an healthy brain.

(c) Affected brain MR $\mathcal{I}$ scan. **(d)** Affected brain, $\mathcal{G}$ image.

Figure 3. Gamma correction results.

3.2. Post-processing

In order to localize the tumor, once the smaller triangles have been selected and the binary map b produced, to better delineate the tumor area and to get rid of the cortex profile as well as any other noisy area, a morphological transformation called erosion (see e.g, Chapter 5 in [44]) is applied with the following kernel:

$$Kernel := \begin{pmatrix} 1 & 1 & 1 \\ 1 & 1 & 1 \\ 1 & 1 & 1 \end{pmatrix}. \tag{8}$$

As the kernel slides through the image, a pixel is considered 1, and hence, white, if all the pixels under the kernel are 1, otherwise it is eroded and its value is set to 0, i.e., black, see Fig.4. The erosion transformation is repeated up to 6 times per image. At the end of this phase, if the resulting image is completely black or if there are spurious white pixels accounting less than 1%, then the considered input MR $\mathcal{I}$ is automatically labelled as "healthy", otherwise, it is automatically labelled as "affected".

The proposed procedure is implemented in `FreeFem ++`, version 3.5, see [45] for the finite-element approximation and is using the openCV[1] Python library for the post-processing step. The tests are performed on a free dataset available on Kaggle [2]. There are in total 215 MR images of different sizes and of different modalities, i.e., T1, T2, but these information are not apriori provided. The affected brains are 155 while the healthy ones

[1] https://github.com/opencv/opencv-python
[2] https://www.kaggle.com/datasets/navoneel/brain-mri-images-for-brain-tumor-detection

 doi:10.20944/preprints202209.0036.v1

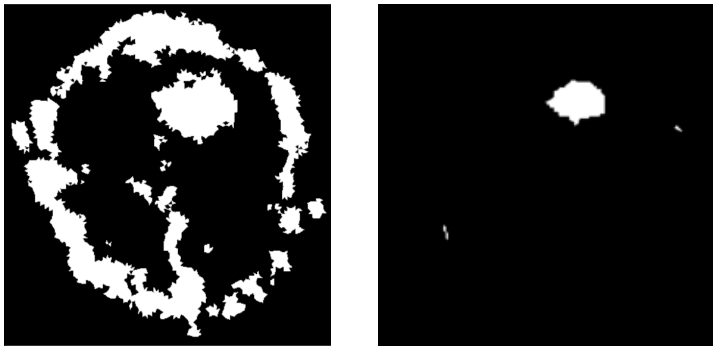

(a) Obtained binary map b from definition (7).

(b) Post-processing result.

Figure 4. Binary map treatment.

are 98. The images come split in two folders for the healthy and the affected ones so that a post evaluation of the performance of the algorithm is possible. In particular, sensitivity and miss rate are considered as indices for the evaluation. By using sensitivity, also called true positive rate, it is possible to see how many brain images, in the affected folder, are correctly labelled, as well as, how many images are correctly classified as healthy, in the other folder. The indicator miss rate instead is giving insight of the wrongly classified images. By observing the results reported in Table 1 it is evident how the proposed strategy is more prone to identify anomalous regions, and hence, to label as "affected", in most of the circumstances, any given input image. To understand better the reasons of this behavior is necessary to analyze the MR scans of healthy brains that were wrongly classified as affected, since this category is the one where the proposed algorithm is rather faulty, i.e., 63.27% of failure.

Table 1. Sensitivity and miss rate for the affected and for the healthy brains.

Index	Affected	Healthy
Sensitivity	92.26%	36.73%
Miss rate	7.74%	63.27%

3.3. Correction

For certain images of healthy brains in the considered dataset, like the T2-weighted MR images, the cerebrospinal fluid appears with a high intensity signal [46], resulting therefore in bright areas, surrounded by dark pixels, that can be easily mistaken for anomalous sites after the gamma correction introduced in subsection 3.1, see the example in Fig. 5.

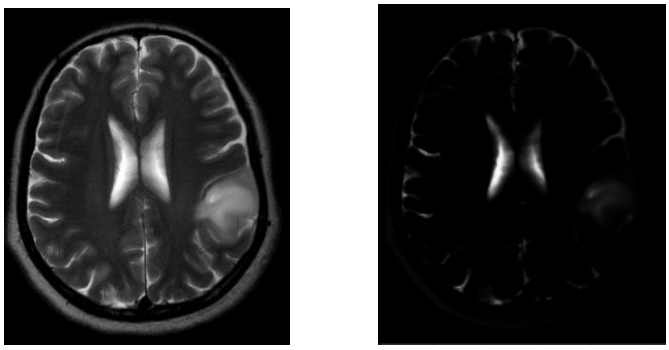

(a) Image id N22: healthy brain.

(b) Image id N22 after gamma correction.

Figure 5. The cerebrospinal fluid appears with high intensity signal for T2-weighted MRIs.

Preprints (www.preprints.org) | NOT PEER-REVIEWED | Posted: 2 September 2022 doi:10.20944/preprints202209.0036.v1

Therefore, for such cases, the image $\mathcal{G}$ is produced by using $\gamma = 1/8$. The results of this operation are shown in Fig. 6. After this type of correction, the sensitivity index for the "healthy" category is increased to 72.45% and the miss rate is reduced to 27.55%.

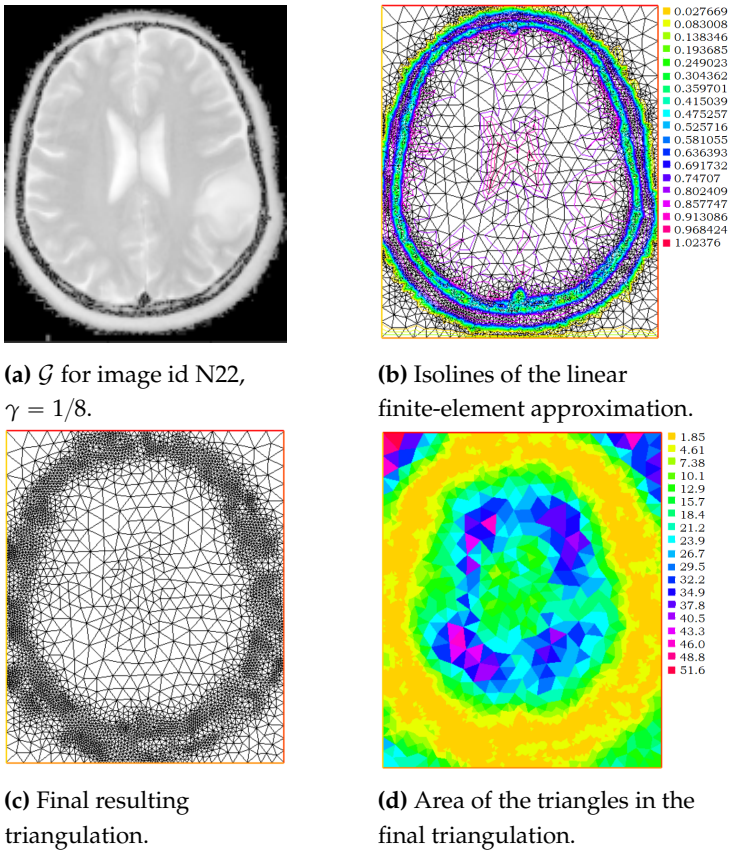

(a) $\mathcal{G}$ for image id N22, $\gamma = 1/8$.

(b) Isolines of the linear finite-element approximation.

(c) Final resulting triangulation.

(d) Area of the triangles in the final triangulation.

Figure 6. Treatment of the T2-weighted MR scans.

The following tests are implemented by using `FreeFem++`, a free finite-elements software.

4. Discussion

The proposed procedure is globally evaluated by using two common metrics: the overall accuracy (OA) and the F_1 score. In particular, denoting with:

- TP: true positive, i.e., affected brains correctly classified;
- TN: true negative, i.e., healthy brains correctly classified;
- FP: false positive, i.e., healthy brains mistakenly classified as affected;
- FN: false negative, i.e., affected brains wrongly classified as healthy;

the overall accuracy is defined as,

$$OA := \frac{TP + TN}{TP + TN + FP + FN},$$

while the F_1 score is computed as,

$$F_1 := \frac{2TP}{2TP + FP + FN}.$$

The obtained results are displayed in Table 2 where also other competitors on the same dataset are shown. In particular, Auto-Encoder [31] and MemAE [47] are based on deep autoencoder architecture; AnoGAN [48], f-AnoGAN [49], GANomaly [50], Sparse-GAN [51], pix2pix [52] and Cycle-GAN [53] are based on generative adversarial networks; Proxy-

Preprints (www.preprints.org) | NOT PEER-REVIEWED | Posted: 2 September 2022 doi:10.20944/preprints202209.0036.v1

Bridged [35] uses an intermediate proxy to bridge the input image and the reconstructed image to detect the anomalous regions.

Table 2. Competitors results on the same analyzed dataset. In bold the best results.

Methods	OA	F_1
Z2-γ	**0.846**	**0.880**
Auto-Encoder	0.714	0.674
MemAE	0.789	0.722
AnoGAN	0.757	0.691
f-AnoGAN	0.764	0.675
GANomaly	0.798	0.667
Sparse-GAN	0.791	0.645
pix2pix	0.737	0.617
Cycle-GAN	0.752	0.712
Proxy-Bridged	0.805	0.709

The results in Table 2 clearly shows the competitiveness of the proposed algorithm with respect to other methods, some of them even developed as supervised approaches, in the tumor detection task.

5. Conclusions

In this paper a method based on finite-elements and on the Z2 error estimator is presented to address the task of tumor detection in brain MR images. The proposed approach is called Z2-γ as it also relies on a suitable preliminary gamma correction which helps to better highlight the anomalous regions, whenever present. This initial study shows promising results in the application of the Z2 error estimator, together with isotropic triangulations, and specific tools of image processing in the automatic detection of brain tumors. Future work is currently devoted to the study of brain-tumor segmentation in its various parts, i.e., active cells, necrotic core, and edema, see e.g., [54–56] and references therein, a task which requires a better discriminative power of the error estimator, as well as suitable input images, see e.g., [57].

Funding: The research of Antonella Falini is founded by PON Project AIM 1852414 CUP H95G18000120006 ATT1 and project CUP H95F21001470001

Acknowledgments: The author thanks the Italian National Group for Scientific Computing (Gruppo Nazionale per il Calcolo Scientifico) for its valuable support under the INDAM-GNCS project CUP_E55F22000270001

Conflicts of Interest: The author declares no conflict of interest. The funders had no role in the design of the study; in the collection, analyses, or interpretation of data; in the writing of the manuscript; or in the decision to publish the results.

References

1. Zienkiewicz, O.C.; Zhu, J.Z. A simple error estimator and adaptive procedure for practical engineerng analysis. *International journal for numerical methods in engineering* **1987**, *24*, 337–357.
2. Zienkiewicz, O.C.; Zhu, J.Z. The superconvergent patch recovery and a posteriori error estimates. Part 1: The recovery technique. *International Journal for Numerical Methods in Engineering* **1992**, *33*, 1331–1364.
3. Zienkiewicz, O.C.; Zhu, J.Z. The superconvergent patch recovery and a posteriori error estimates. Part 2: Error estimates and adaptivity. *International Journal for Numerical Methods in Engineering* **1992**, *33*, 1365–1382.
4. Bourdin, B. Image segmentation with a finite element method. *ESAIM: Mathematical modelling and numerical analysis* **1999**, *33*, 229–244.
5. Chiappa, A.S.; Micheletti, S.; Peli, R.; Perotto, S. Mesh adaptation-aided image segmentation. *Communications in Nonlinear Science and Numerical Simulation* **2019**, *74*, 147–166.
6. Clerici, F.; Ferro, N.; Marconi, S.; Micheletti, S.; Negrello, E.; Perotto, S. Anisotropic adapted meshes for image segmentation: Application to three-dimensional medical data. *SIAM Journal on Imaging Sciences* **2020**, *13*, 2189–2212.

7. Giacomini, M.; Perotto, S. Anisotropic mesh adaptation for region-based segmentation accounting for image spatial information. *Computers & Mathematics with Applications* **2022**, *121*, 1–17.
8. Yaacobson, F.S.; Givoli, D. An adaptive finite element procedure for the image segmentation problem. *Communications in numerical methods in engineering* **1998**, *14*, 621–632.
9. Amin, J.; Sharif, M.; Raza, M.; Saba, T.; Anjum, M.A. Brain tumor detection using statistical and machine learning method. *Computer methods and programs in biomedicine* **2019**, *177*, 69–79.
10. Sharif, M.; Amin, J.; Raza, M.; Anjum, M.A.; Afzal, H.; Shad, S.A. Brain tumor detection based on extreme learning. *Neural Computing and Applications* **2020**, *32*, 15975–15987.
11. Seetha, J.; Raja, S.S. Brain tumor classification using convolutional neural networks. *Biomedical & Pharmacology Journal* **2018**, *11*, 1457.
12. Othman, M.F.; Basri, M.A.M. Probabilistic neural network for brain tumor classification. In Proceedings of the 2011 Second International Conference on Intelligent Systems, Modelling and Simulation. IEEE, 2011, pp. 136–138.
13. Sapra, P.; Singh, R.; Khurana, S. Brain tumor detection using neural network. *International Journal of Science and Modern Engineering (IJISME) ISSN* **2013**, pp. 2319–6386.
14. Amin, J.; Sharif, M.; Yasmin, M.; Fernandes, S.L. Big data analysis for brain tumor detection: Deep convolutional neural networks. *Future Generation Computer Systems* **2018**, *87*, 290–297.
15. Dong, H.; Yang, G.; Liu, F.; Mo, Y.; Guo, Y. Automatic brain tumor detection and segmentation using U-Net based fully convolutional networks. In Proceedings of the annual conference on medical image understanding and analysis. Springer, 2017, pp. 506–517.
16. Abdel-Maksoud, E.; Elmogy, M.; Al-Awadi, R. Brain tumor segmentation based on a hybrid clustering technique. *Egyptian Informatics Journal* **2015**, *16*, 71–81.
17. Alam, M.S.; Rahman, M.M.; Hossain, M.A.; Islam, M.K.; Ahmed, K.M.; Ahmed, K.T.; Singh, B.C.; Miah, M.S. Automatic human brain tumor detection in MRI image using template-based K means and improved fuzzy C means clustering algorithm. *Big Data and Cognitive Computing* **2019**, *3*, 27.
18. Islam, M.K.; Ali, M.S.; Miah, M.S.; Rahman, M.M.; Alam, M.S.; Hossain, M.A. Brain tumor detection in MR image using superpixels, principal component analysis and template based K-means clustering algorithm. *Machine Learning with Applications* **2021**, *5*, 100044.
19. Kaur, N.; Sharma, M. Brain tumor detection using self-adaptive K-means clustering. In Proceedings of the 2017 International Conference on Energy, Communication, Data Analytics and Soft Computing (ICECDS). IEEE, 2017, pp. 1861–1865.
20. Malathi, M.; Sinthia, P. MRI brain tumour segmentation using hybrid clustering and classification by back propagation algorithm. *Asian Pacific Journal of Cancer Prevention: APJCP* **2018**, *19*, 3257.
21. Selvy, P.T.; Palanisamy, V.; Purusothaman, T. Performance analysis of clustering algorithms in brain tumor detection of MR images. *European Journal of Scientific Research* **2011**, *62*, 321–330.
22. Akram, M.U.; Usman, A. Computer aided system for brain tumor detection and segmentation. In Proceedings of the International conference on Computer networks and information technology. IEEE, 2011, pp. 299–302.
23. Amin, J.; Sharif, M.; Yasmin, M.; Fernandes, S.L. A distinctive approach in brain tumor detection and classification using MRI. *Pattern Recognition Letters* **2020**, *139*, 118–127.
24. Hedberg, H.; Kristensen, F.; Nilsson, P.; Owall, V. A low complexity architecture for binary image erosion and dilation using structuring element decomposition. In Proceedings of the 2005 IEEE International Symposium on Circuits and Systems. IEEE, 2005, pp. 3431–3434.
25. Lemieux, L.; Hagemann, G.; Krakow, K.; Woermann, F.G. Fast, accurate, and reproducible automatic segmentation of the brain in T1-weighted volume MRI data. *Magnetic Resonance in Medicine: An Official Journal of the International Society for Magnetic Resonance in Medicine* **1999**, *42*, 127–135.
26. Mustaqeem, A.; Javed, A.; Fatima, T. An efficient brain tumor detection algorithm using watershed & thresholding based segmentation. *International Journal of Image, Graphics and Signal Processing* **2012**, *4*, 34.
27. Prajapati, S.J.; Jadhav, K.R. Brain tumor detection by various image segmentation techniques with introduction to non negative matrix factorization. *Brain* **2015**, *4*, 600–603.
28. Nabizadeh, N.; John, N.; Wright, C. Histogram-based gravitational optimization algorithm on single MR modality for automatic brain lesion detection and segmentation. *Expert systems with applications* **2014**, *41*, 7820–7836.
29. Nabizadeh, N.; Kubat, M. Brain tumors detection and segmentation in MR images: Gabor wavelet vs. statistical features. *Computers & Electrical Engineering* **2015**, *45*, 286–301.
30. Borole, V.Y.; Nimbhore, S.S.; Kawthekar, D.S.S. Image processing techniques for brain tumor detection: A review. *International Journal of Emerging Trends & Technology in Computer Science (IJETTCS)* **2015**, *4*, 2.
31. Baur, C.; Wiestler, B.; Albarqouni, S.; Navab, N. Deep autoencoding models for unsupervised anomaly segmentation in brain MR images. In Proceedings of the International MICCAI brainlesion workshop. Springer, 2018, pp. 161–169.
32. Baur, C.; Wiestler, B.; Albarqouni, S.; Navab, N. Bayesian skip-autoencoders for unsupervised hyperintense anomaly detection in high resolution brain MRI. In Proceedings of the 2020 IEEE 17th International Symposium on Biomedical Imaging (ISBI). IEEE, 2020, pp. 1905–1909.

33. Chen, X.; You, S.; Tezcan, K.C.; Konukoglu, E. Unsupervised lesion detection via image restoration with a normative prior. *Medical image analysis* **2020**, *64*, 101713.
34. Han, C.; Rundo, L.; Murao, K.; Noguchi, T.; Shimahara, Y.; Milacski, Z.Á.; Koshino, S.; Sala, E.; Nakayama, H.; Satoh, S. MADGAN: Unsupervised medical anomaly detection GAN using multiple adjacent brain MRI slice reconstruction. *BMC bioinformatics* **2021**, *22*, 1–20.
35. Zhou, K.; Li, J.; Luo, W.; Li, Z.; Yang, J.; Fu, H.; Cheng, J.; Liu, J.; Gao, S. Proxy-bridged Image Reconstruction Network for Anomaly Detection in Medical Images. *IEEE Transactions on Medical Imaging* **2021**, *41*, 582–594.
36. Zimmerer, D.; Isensee, F.; Petersen, J.; Kohl, S.; Maier-Hein, K. Unsupervised anomaly localization using variational auto-encoders. In Proceedings of the International Conference on Medical Image Computing and Computer-Assisted Intervention. Springer, 2019, pp. 289–297.
37. Michael Mahesh, K.; Arokia Renjit, J. Evolutionary intelligence for brain tumor recognition from MRI images: a critical study and review. *Evolutionary Intelligence* **2018**, *11*, 19–30.
38. Dörfler, W. A convergent adaptive algorithm for Poisson's equation. *SIAM Journal on Numerical Analysis* **1996**, *33*, 1106–1124.
39. Morin, P.; Nochetto, R.H.; Siebert, K.G. Data oscillation and convergence of adaptive FEM. *SIAM Journal on Numerical Analysis* **2000**, *38*, 466–488.
40. Ding, S.; Shao, G.; Huang, Y.; Shi, H. The superconvergence gradient recovery method for linear finite element method with polygons. *International Journal for Numerical Methods in Engineering* **2021**, *122*, 4154–4171.
41. Maisano, G.; Micheletti, S.; Perotto, S.; Bottasso, C.L. On some new recovery-based a posteriori error estimators. *Computer methods in applied mechanics and engineering* **2006**, *195*, 4794–4815.
42. Rodríguez, R. Some remarks on Zienkiewicz-Zhu estimator. *Numerical Methods for Partial Differential Equations* **1994**, *10*, 625–635.
43. Zhang, Z.; Naga, A. A new finite element gradient recovery method: superconvergence property. *SIAM Journal on Scientific Computing* **2005**, *26*, 1192–1213.
44. Haralick, R.M.; Shapiro, L.G. *Computer and robot vision*; Vol. 1, Addison-wesley Reading, 1992.
45. Hecht, F. New development in FreeFem++. *J. Numer. Math.* **2012**, *20*, 251–265.
46. Lisanti, C.; Carlin, C.; Banks, K.P.; Wang, D. Normal MRI appearance and motion-related phenomena of CSF. *American Journal of Roentgenology* **2007**, *188*, 716–725.
47. Gong, D.; Liu, L.; Le, V.; Saha, B.; Mansour, M.R.; Venkatesh, S.; Hengel, A.v.d. Memorizing normality to detect anomaly: Memory-augmented deep autoencoder for unsupervised anomaly detection. In Proceedings of the Proceedings of the IEEE/CVF International Conference on Computer Vision, 2019, pp. 1705–1714.
48. Schlegl, T.; Seeböck, P.; Waldstein, S.M.; Schmidt-Erfurth, U.; Langs, G. Unsupervised anomaly detection with generative adversarial networks to guide marker discovery. In Proceedings of the International conference on information processing in medical imaging. Springer, 2017, pp. 146–157.
49. Schlegl, T.; Seeböck, P.; Waldstein, S.M.; Langs, G.; Schmidt-Erfurth, U. f-AnoGAN: Fast unsupervised anomaly detection with generative adversarial networks. *Medical image analysis* **2019**, *54*, 30–44.
50. Akcay, S.; Atapour-Abarghouei, A.; Breckon, T.P. Ganomaly: Semi-supervised anomaly detection via adversarial training. In Proceedings of the Asian conference on computer vision. Springer, 2018, pp. 622–637.
51. Zhou, K.; Gao, S.; Cheng, J.; Gu, Z.; Fu, H.; Tu, Z.; Yang, J.; Zhao, Y.; Liu, J. Sparse-gan: Sparsity-constrained generative adversarial network for anomaly detection in retinal oct image. In Proceedings of the 2020 IEEE 17th International Symposium on Biomedical Imaging (ISBI). IEEE, 2020, pp. 1227–1231.
52. Isola, P.; Zhu, J.Y.; Zhou, T.; Efros, A.A. Image-to-image translation with conditional adversarial networks. In Proceedings of the Proceedings of the IEEE conference on computer vision and pattern recognition, 2017, pp. 1125–1134.
53. Zhu, J.Y.; Park, T.; Isola, P.; Efros, A.A. Unpaired image-to-image translation using cycle-consistent adversarial networks. In Proceedings of the Proceedings of the IEEE international conference on computer vision, 2017, pp. 2223–2232.
54. Liu, J.; Li, M.; Wang, J.; Wu, F.; Liu, T.; Pan, Y. A survey of MRI-based brain tumor segmentation methods. *Tsinghua science and technology* **2014**, *19*, 578–595.
55. Tiwari, A.; Srivastava, S.; Pant, M. Brain tumor segmentation and classification from magnetic resonance images: Review of selected methods from 2014 to 2019. *Pattern Recognition Letters* **2020**, *131*, 244–260.
56. Wadhwa, A.; Bhardwaj, A.; Verma, V.S. A review on brain tumor segmentation of MRI images. *Magnetic resonance imaging* **2019**, *61*, 247–259.
57. De Nunzio, G.; Pastore, G.; Donativi, M.; Castellano, A.; Falini, A. A CAD system for cerebral glioma based on texture features in DT-MR images. *Nuclear Instruments and Methods in Physics Research Section A: Accelerators, Spectrometers, Detectors and Associated Equipment* **2011**, *648*, S100–S102.